Presented at the UEF Conference on Turbulent Heat Transfer III, Girdwood, Alaska, March 18-22, 2001

# The Effect of Walls on Turbulent Flow and Temperature Fields

*Naoya FUKUSHIMA and Nobuhide KASAGI*

Department of Mechanical Engineering, The University of Tokyo
Hongo 7-3-1, Bunkyo-ku, Tokyo 113-8656, Japan

## 1. Introduction

Turbulent heat transfer is of great importance in a wide range of engineering applications. In many turbomachines and heat exchangers, conduits of complex geometry are used to improve the heat transfer and pressure loss. It is known that a solid wall makes Reynolds stresses anisotropic and inhomogeneous through its no-slip and impermeable conditions. The anisotropy and inhomogeneity of the near-wall stresses would cause secondary flows of the Prandtlís second kind and consequently alter the turbulence structure. Their effect on momentum and heat transfer is significant. Hence, for designing more efficient fluid and thermal mechanical equipment, it is crucial to understand the underlying physical mechanism of the wall effects, and to develop turbulence models, with which we can predict complex flow and heat transfer with sufficiently high accuracy.

Over the decades, a number of investigations have been carried out both numerically and experimentally to explore the effect of the walls on turbulent flow and temperature fields. However, most of them are concerned with a single plane boundary, which does not involve geometrical complexity such as corners, apexes and wavy walls. An exception is studies on turbulent flow in a non-circular duct. For instance, Gavrilakis (1992) and Huser and Biringen (1993) performed direct numerical simulation (DNS, hereafter) of fully developed turbulent flows in a square duct at low Reynolds numbers. Using the statistics of turbulent velocity field obtained, they clarified the influence of the duct corner on the stress anisotropy and discussed the origin of the secondary flow of the second kind. However, to the best of the authorsí knowledge, there is no literature reporting DNS data of associated turbulent temperature field. As for experimental studies, there are only two on a smooth square duct reported by Brundrett and Burroughs (1967) and Hirota *et al*. (1997), while others seem to have paid more attention to a rough-wall duct. Despite these investigations, the understanding of the effect of the presence of two intersecting walls on turbulent transport mechanism is neither complete nor satisfactory. In the present work, we study the fully developed turbulent velocity and temperature fields in square and diamond ducts, where the corners of different angles would cause distinct wall effects.

## 2. Numerical Procedure

The flow geometry and the coordinate systems are shown in Figs. 1 and 2. The computational domain size is $5\pi\delta$ x $2\delta$ x $2\delta$ for a square duct, and $5\pi\delta\times4/\sqrt{3}\delta\times4/\sqrt{3}\delta$ for a diamond duct with 128 x 65 x 65 grid points in the $x_1$, $x_2$ and $x_3$ directions. The Reynolds number, $\mathrm{Re}_b$, based on the mean streamwise velocity $U_b$ and the hydrodynamic diameter $D$, i.e., the duct width $2\delta$, is set to be 4485. No-slip condition is imposed on the walls and the periodic condition is applied at the streamwise boundaries. The Navier-Stokes and energy equations are integrated in time by using the fractional step method (Kim & Moin, 1984). Temperature is considered as a passive scalar with the Prandtl number of the fluid being 0.71. The wall temperature is assumed to be constant along the sides of the duct at a local streamwise position, but it is assumed to increase linearly in the streamwise direction. In other words, the wall surface is isothermal at any cross section normal to the duct axis, and the wall heat flux is uniform in the streamwise direction, so that the difference between the bulk-mean and wall temperatures is always kept constant.

For time advancement, the third-order Runge-Kutta (Spalart *et al.*, 1991) and Crank-Nicolson schemes

are adopted for the advection and viscous terms, respectively. The spatial discretization is made by a second-order finite volume method using a collocated mesh system in the generalized curvilinear coordinate system. Once the velocity field is advanced for each time step, the scalar field is obtained by integrating the energy equation (Akselvoll and Moin, 1995).

## 3. Results and Discussion

### 3.1 Mean flow and heat transfer properties in square and diamond ducts

Figures 3 and 4 show the contour maps of the time-averaged streamwise velocity, $U/U_b$, in the square and diamond duct, respectively. The subscript of $b$ means the bulk mean value. Since the induced secondary flow transports high momentum fluid from the center to the corner of the duct, the contours are distorted accordingly. In the diamond duct, the contours are distorted more strongly near the corners of obtuse angle. The distribution of the mean temperature is very similar to that of the mean streamwise velocity in both ducts, although the deformation of the former is somewhat smaller than that of the latter. This suggests that the enhancement of heat transfer by the secondary flow is weaker than that of momentum transport. Similar phenomena have also been observed in the experiment of a square duct at higher Reynolds number by Hirota *et al*. (1997).

Figures 5 and 6 show the mean secondary flows in the square and diamond ducts, respectively. In the square duct, a pair of counter-rotating vortices appear in every corner because of the symmetry of the square duct. In the diamond duct, however, a pair of larger counter-rotating vortices appear near the corners of acute angle (Corner A), and their centers are further away from the corner. The vortices are strongly distorted and can not reach the corner. On the other hand, near the corners of obtuse angle (Corner B), there appear a pair of smaller counter-rotating vortices, the centers of which are closer to the corner. These facts imply that the enhancement of turbulent heat and momentum transfer by the secondary flow is stronger near Corner B than near Corner A.

The friction factor and the Nusselt number are defined as follows:

$$f = 8u_\tau^2 / U_b^2 = \frac{8}{\mathrm{Re}_b}\left[\frac{d(U/U_b)}{d(x_2/D)}\right]_{x_2=0} \tag{1}$$

$$Nu = \frac{hD}{\lambda} = \left[\frac{d(T/T_b)}{d(x_2/D)}\right]_{x_2=0} \tag{2}$$

Their mean values, $f_0$ and $Nu_0$, which have been obtained by averaging Eqs. (1) and (2) over the side length, are shown in Table 1. For comparison, those of a circular duct at $\mathrm{Re}_b$ = 4300 (Satake *et al*., 2000) are also included. In order to compensate a slight difference in the bulk Reynolds numbers among these data, the ratio of $Nu/(f\,\mathrm{Re}_b)$ is also listed in Table 1. It is clear that, in view of heat transfer augmentation, the diamond duct gives the best performance, while the circular duct is the second best.

The normalized local friction parameter, $f/f_0$, and Nusselt number, $Nu/Nu_0$, in the square and diamond ducts are shown in Figs. 7 and 8, respectively. In the square duct, $f/f_0$ is larger than $Nu/Nu_0$ in the region close to the corner, while the opposite trend is observed near the center of the wall. In the diamond duct, near Corner B, where the turbulent heat and momentum transfer is enhanced more strongly by the secondary flow, both $f/f_0$ and $Nu/Nu_0$ are larger than those near Corner A. Note that $Nu/Nu_0$ is larger than $f/f_0$ near Corner B. Thus, from a viewpoint of heat transfer equipment, the duct which has obtuse-angle corners should be more efficient than that which has acute-angle corners. For example, it is expected that a hexagonal duct with only obtuse-angle corners gives good heat transfer properties.

### 3.2 Reynolds stress and turbulent heat flux in square and diamond ducts

The contour maps of the turbulent heat flux in the $x_2$-direction, $\overline{u_2 t}$, in the square and diamond ducts are shown in Figs. 9 and 10, respectively. The turbulent heat flux is normalized by the bulk mean streamwise

velocity, $U_b$, and the bulk mean temperature, $T_b$. Near the bottom wall, the component of $u_2$ has the property of wall-normal velocity. Therefore, the turbulent heat flux of $\overline{u_2 t}$ is expected to mainly contribute to the turbulent heat transfer near the bottom wall. In both ducts, $\overline{u_2 t}$ is zero on the bottom wall surface, but its magnitude increases very rapidly to 0.004 at $x_2 / D = 0.1$. It is strongly damped by both side walls in the square duct. In the diamond duct, however, $\overline{u_2 t}$ is damped more strongly near Corner A (with the acute angle) than near Corner B (with the obtuse angle), so that the maximum magnitude of $\overline{u_2 t}$ appears close to corner B.

It is separately confirmed that the distribution of $\overline{u_2 t}$ is qualitatively very similar to that of the Reynolds stress, $\overline{u_1 u_2}$ (not shown), but the absolute value of the former is larger than that of the latter, especially near the bottom wall in the square duct and near Corner B in the diamond duct. The maximum magnitude of $\overline{u_1 u_2}$ normalized by the mean streamwise velocity, $U_b$, are 0.00369 and 0.00375 in the square and diamond ducts, respectively. These are the reasons why the friction parameter, $f/f_0$, and the Nusselt number, $Nu/Nu_0$, are distributed in a somewhat dissimilar manner as has been shown in Figs. 7 and 8.

In the square duct, the signs of both $\overline{u_2 t}$ and $\overline{u_1 u_2}$ are reversed near the side walls, where the component of $u_2$ has the property of wall-parallel velocity. In the diamond duct, these signs are reversed only near the side wall with the obtuse angle, while both signs remain negative near the side wall with the acute angle. However, near both side walls, the $x_2$-direction have both properties of transverse and wall-normal directions.

### 3.3 Generalized coordinate system based on the principal axes of Reynolds stress

As described above, the components of $u_2$ and $u_3$ have both properties of the wall-normal and transverse velocities in the square and diamond ducts, where the wall-normal direction is ambiguous in its physical sense because of the existence of two intersecting walls. Hence, a question arises whether the conventional Cartesian coordinate system is appropriate to investigate turbulent flow and temperature fields and understand the physical mechanism in a complex geometry. To resolve this issue, we employ a generalized coordinate system, where we define the three normal directions based on principal axes of the local Reynolds stress tensor. The direction of $x_s$, which contains the largest normal stress, is used instead of the $x_1$-direction, whilst the direction of $x_n$, which holds the least normal stress, and that of $x_t$, which is normal to other two directions, are employed instead of the $x_2$- and $x_3$-directions. In other words, these directions correspond to the eigenvectors of Reynolds stress $\overline{u_i u_j}$. The unit vector in the $x_s$-direction is the eigenvector with the largest eigenvalue of $\overline{u_i u_j}$ and that in the $x_n$-direction is the eigenvector with the smallest eigenvalue.

It is found that the $x_s$-direction is nearly parallel to the streamwise direction, but inclined to the closest wall at a small angle in the square and diamond ducts (not shown).

As shown in Fig. 11, in the square duct, the $x_n$-direction appears nearly normal to the closest wall, except for the diagonal region of the duct, and inclined to the streamwise direction at a small angle near the wall. Figure 12 shows the $x_n$-direction in the diamond duct. The $x_n$-direction in the diamond duct has the similar distribution to that in the square duct. This fact suggests that it is a good approximation to employ wall damping turbulence models which are a function of the distance from the closest wall even in relatively complex geometry, such as square and diamond ducts.

The $x_t$-direction is nearly normal to the $x_n$-direction in the $x_2$-$x_3$ cross section, and is still parallel to the closest wall in the square and diamond ducts (not shown).

Thus, the eigenvectors of Reynolds stresses seem to have the same physical properties in both square and diamond ducts, and they are likely to serve as a rather universal measure near walls of various shapes.

### 3.4 Anisotropy tensor of Reynolds stress on generalized coordinate system

The above proposed generalized coordinate system is applied to the stress anisotropy tensor, $b_{ij} = \overline{u_i u_j} / 2k - 1/3$, in the square duct. The contour map of the anisotropy tensor component of $b_{22}$ is shown in Fig. 13. Similarly to the turbulent heat flux of $\overline{u_2 t}$, $b_{22}$ has both the properties of the wall-normal and transverse turbulent velocity components. The distribution of $b_{33}$ is symmetric to that of $b_{22}$.

The distribution of $b_{ss}$ is very similar to that of $b_{11}$ because reynolds stress, $\overline{u_1 u_1}$, is much larger than

any other reynolds stresses and the $x_s$ -direction is nearly parallel to the streamwise direction. Figures 14 and 15 show the contour maps of $b_{nn}$ and $b_{tt}$. Judging from the direction of the corresponding eigenvectors, $b_{nn}$ has only the property of wall-normal velocity component, whilst $b_{tt}$ represents only that of transverse velocity component. The characteristics of wall-normal and transverse velocity components can be clearly understood.

According to the definition, the value of $b_{nn}$ is smaller than that of $b_{tt}$ all over the cross section of the duct. The contours of $b_{nn}$ bulge toward the duct corner on the diagonal. This means that the anisotropy of $\overline{u_n u_n}$ is weak along the diagonal lines although $u_n$ is strongly suppressed by the effect of corner walls. On the other hand, the $b_{tt}$ contours are distorted toward the wall around the wall bisector. As the wall is approached, except for the duct corner, the anisotropy tensor component of $b_{nn}$ is decreasing, but $b_{tt}$ is increasing. Consequently, two-component turbulence is found near the wall. In the region immediate to the corner, $b_{tt}$ and $b_{nn}$ become as small as -1/3 and hence one-component turbulence is developed. This damping effect of the two intersecting walls is limited in a very narrow region.

**3.5 Stress production terms in generalized coordinate system**

The effects of walls on the Reynolds stresses are revisited from a viewpoint of the production terms in their transport equation. In the conventional Cartesian coordinate system, the production and redistribution mechanisms of the Reynolds stresses is explained, for example, in the case of a simple plane channel, as:

1) the streamwise normal Reynolds stress, $\overline{u_1 u_1}$, and the primary shear Reynolds stress, $\overline{u_1 u_2}$, are produced by a mean velocity gradient $dU_1/dx_2$, where $\overline{u_1 u_1}$ and $\overline{u_1 u_2}$ are related with each other through the production terms,
2) the normal Reynolds stresses in the other directions, i.e., $\overline{u_2 u_2}$ and $\overline{u_3 u_3}$, are transformed from the streamwise normal stress through the pressure-strain correlation terms.

Therefore, the accurate prediction of the Reynolds stresses requires comprehensive understanding of the complex interactions among different components of the Reynolds stresses including the off-diagonal components, which are not conservative quantities.

On the other hand, the diagonal components of the production terms can be simply written by using the present generalized coordinate system, i.e.,

$$P_{\alpha\alpha} = -2\overline{u_\alpha u_\alpha}\partial U_\alpha / \partial x_\alpha = -2\overline{u_\alpha u_\alpha} S_{\alpha\alpha} \quad (\alpha = s, n \text{ or } t) \tag{4}$$

because of the normalization of Reynolds stress tensor. Namely, $P_{\alpha\alpha}$ is the production only of the normal Reynolds stress in each direction, $\overline{u_\alpha u_\alpha}$, and the mean velocity gradient, $\partial U_\alpha / \partial x_\alpha$. Moreover, Eq. (4) is further simplified by the fact that the mean velocity gradient, $\partial U_\alpha / \partial x_\alpha$, is equal to the mean rate of strain, $S_{\alpha\alpha}$.

Using this expression, it is possible to distinguish the mean velocity gradient that is directly related with the production of turbulent kinetic energy. The mean rates of strain, $S_{ss}$, $S_{nn}$ and $S_{sn}$, are shown in Figs. 16, 17 and 18, respectively. Absolute values of other three components are relatively small. It is found that $S_{sn}$ is much larger than all other components, but does not directly produce the turbulent kinetic energy as easily understood from Eq. (4). Negative values of $S_{ss}$ indicate the enhancement of $\overline{u_s u_s}$, particularly near the wall except for the corner. In contrast with $S_{ss}$, $S_{nn}$ suppresses $\overline{u_n u_n}$ near the wall except for the corner. The absolute value of $S_{tt}$ is small. As a result, $S_{ss}$, $S_{nn}$ and $S_{tt}$ as a whole contribute to the anisotropy and inhomogeneity of the Reynolds stresses in the $x_s$, $x_n$ and $x_t$ -directions.

The contour maps of both $S_{ss}$ and $S_{nn}$ are distorted toward the corner. The production terms of $\overline{u_s u_s}$ and $\overline{u_n u_n}$ are small near the diagonal lines. This is one of the reasons why the anisotropy of $\overline{u_n u_n}$ is weak along the diagonal line, although $u_n$ is strongly suppressed by the effect of walls near the corner, as shown in Fig. 15.

Equation (4) implies the normal Reynolds stresses depend neither upon the mean vorticity tensors nor the off-diagonal mean strain rates, $S_{\alpha\beta}$ ($\alpha \neq \beta$), but only on the diagonal strain rate, $S_{\alpha\alpha}$. Based on these discussions, one can expect the Reynolds stresses be written as simpler functions of mean rates of strain in this generalized coordinate system.

**3.6 Turbulence modeling using generalized coordinate system**

To demonstrate the merits in employing the present coordinate system as compared to the Cartesian coordinate system, we use the linear *k*-ε model as an example and compare the behavior of the proportional constants, $c_{\mu ij}$, in these coordinate systems. The *k*-ε model in the Cartesian coordinate system can be written as:

$$-\overline{u_i u_j} + \frac{2}{3}\delta_{ij}k = \nu_{tij}\left(\frac{\partial U_i}{\partial x_j} + \frac{\partial U_j}{\partial x_i}\right) = 2c_{\mu_{ij}}\frac{k^2}{\varepsilon}\overline{S_{ij}} \tag{5}$$

while in the present coordinate system,

$$-\overline{u_i u_i} + \frac{2}{3}\delta_{ii}k = 2c_{\mu_{ii}}\frac{k^2}{\varepsilon}\overline{S_{ii}} \quad (i = s \text{ or } n) \tag{6}$$

First, we investigate a regular plane channel flow, where $y^+$ represents the distance from the wall. The proportional constants, $c_{\mu 12}$, in the conventional Cartesian coordinate, and $c_{\mu ss}$ and $c_{\mu nn}$ in this generalized coordinate system, are shown in Figs. 19 and 20, respectively. In both cases, the results are obtained from the DNS data by Kuroda (1990) at $\mathrm{Re}_\tau = 150$, based on $u_\tau$ and the channel half width $\delta$. In the Cartesian coordinate system, $c_{\mu 12}$ has an almost constant value from the center of the channel to $y^+ = 60$ and decreases dramatically toward the wall. It reaches nearly zero near the wall. This is the reason why the wall damping function is necessary for the *k*-ε models. In the generalized coordinate system, however, $c_{\mu ss}$ has an almost constant value of about 0.4 over a range of $y^+ = 70$-110. It increases toward the wall, and reaches the local maximum of 0.6 at $y^+ = 30$. The magnitude of variation of model constants seems much smaller in the generalized coordinate system than in the Cartesian coordinate system. Note that $c_{\mu nn}$ also has a constant value of 0.3 over the channel cross section except for the regions near the wall and the channel center. Since the Reynolds stresses are very small in the vicinity of the wall, say $y^+ < 10$, the deviation from the constant value in that region is not much important.

Figure 20 illustrates that $c_{\mu ss}$ is larger than $c_{\mu nn}$ in the entire domain. The reason is that the kinetic energy in the $x_n$ direction is transformed into that in the $x_s$ direction through pressure strain correlation terms near the wall. Another reason, which can be found only in the present generalized coordinate system, is that the production term of $\overline{u_s u_s}$, i.e., $P_{ss}$, increases as the enhancement of $\overline{u_s u_s}$, while $P_{nn}$ decreases as the suppression of $\overline{u_n u_n}$.

The behavior of $c_{\mu ss}$ and $c_{\mu nn}$ in the square duct is studied in Figs. 21 and 22. The distributions of constants are very similar to those in the plane channel, both qualitatively and quantitatively, except for the corner, $x_2^+ \text{ or } x_3^+ \geq 70$. Hence, over a wide region the same mechanism as in the single plane wall contributes to the production of the anisotropy and inhomogeneity of the Reynolds stresses. In contrast, $c_{\mu ss}$ and $c_{\mu nn}$ are much larger at $x_2^+, x_3^+ \leq 70$ and the maximum values appear around $x_2^+ = x_3^+ = 40$. It means that the anisotropy of the Reynolds stresses is more enhanced if compared with that of the mean strain rates. The mechanisms for this strong anisotropy of the Reynolds stresses are unknown. One possible reason may be that the production terms are not dominant because of the small velocity gradients near the corner bisector, as shown in Figs. 16 and 17.

The model constants of $c_{\mu 13}$ and $c_{\mu 22}$ in the conventional Cartesian coordinate system are shown in Figs. 23 and 24. The distribution of $c_{\mu 13}$ is similar to that of $c_{\mu 12}$ in the plane channel (see Fig. 19) at $x_2^+ \geq x_3^+, x_2^+ \geq 40$. However, $c_{\mu 22}$ and $c_{\mu 13}$ have negative values and show asymmetric distributions with regard to the corner bisector. Their distributions seem to be more complicated than those of $c_{\mu ss}$ and $c_{\mu nn}$.

Frame-invariant turbulence models have been developed and now are being widely used. They are

classified into two kinds of groups: 1) the nonlinear *k*-ε models including explicitly algebraic Reynolds stress models; 2) Reynolds stress transport (or second-order) equation models. These models cannot explicitly include parameters representing geometrical configurations of conduits, such as the distance from a wall, in order to keep the frame-invariant condition. In addition, these models have to predict all Reynolds stress components including the off-diagonal ones and their model constants have to be valid in any coordinate system. These requirements make any frame-invariant turbulence model highly complicated.

Introduction of the present generalized coordinate system seems to have potential to reduce such complexity in turbulence modeling. It is expected that eigenvectors of Reynolds stresses can be easily determined particularly near the wall through geometrical configurations. It is because they have a relatively universal property near the wall even in complex geometry as mentioned previously. This is quite contrary to the conventional frame-invariant nonlinear *k*-ε model, which is to determine the eigenvectors of the Reynolds stresses by nonlinear terms including both mean strain rate and vorticity tensors. In addition, it is sufficient to model only the two normal Reynolds stresses, e.g., $\overline{u_s u_s}$ and $\overline{u_n u_n}$ , and the turbulent kinetic energy in the generalized coordinate system. Namely, it is not necessary to deal with the non-conservative shear Reynolds stresses and $\overline{u_t u_t}$ . Furthermore, the distributions of $c_{\mu ii}$ are simpler in this generalized coordinate system than that in the conventional Cartesian coordinate system. Therefore, it is tactically convincing to take advantage of geometrical configurations to determine the eigenvectors of the Reynolds stresses and to develop a turbulence model in the generalized coordinate system, which is based on the magnitude of normal Reynolds stresses.

**3.7 Prediction of turbulent heat flux in generalized coordinate system**

It is known that, in the conventional Cartesian coordinate system, $\overline{u_1 t}/\overline{u_1 u_1} < 1$, but $\overline{u_2 t}/\overline{u_1 u_2} > 1$ near a single plane wall, such as in a channel. The ratios between normal reynolds stresses and turbulent heat fluxes depend on the directions. Therefore, it seems to be difficult to find a universal law, particularly in complex geometry, where the coordinate directions do not carry any firm physical meaning. To overcome this problem, the use of the direction of turbulent heat flux vector, $x_h$, is proposed (Abe & Suga, 2001). Because only $u_h$ is correlated with *t*, it should be reasonable to consider the correlation between the turbulent heat flux, $\overline{u_h t}$, and the Reynolds stress, $\overline{u_h u_h}$ , rather than that between $\overline{u_1 u_2}$ and $\overline{u_2 t}$ .

First, the directions of turbulent heat flux vector, $x_h$, are examined in a channel flow. Figure 25 shows angles of between the $x_h$- and $x_s$- directions and the streamwise $x_1$-direction. The data used here are at different Prandtl numbers, Pr = 0.71 (Kasagi *et al*., 1991) and Pr = 0.025 (Kasagi *et al*., 1993) with isoflux walls, and also at Pr = 0.71 with isothermal wall (Kasagi & Iida, 1999). The $x_h$-direction aligns with the $x_s$-direction very well, at least near the wall, when the Prandtl number is not far from unity. Note that the deviation of the $x_h$ and $x_s$ directions toward the center of the channel in the isothermal channel is due to the dissimilarity in the boundary conditions for the velocity and temperature fields.

The distributions of the angle, α, between $x_s$- and $x_h$-directions in the square and diamond ducts are shown in Figs. 26 and 27, respectively. The maximum value of α reaches 9 degrees near the corner in the square duct and 11 degrees near the acute-angle corner in the diamond duct. However, the magnitude of turbulent heat flux is very small there. Hence, it is sufficient to predict only $\overline{u_s t}$ accurately.

The distributions of the ratio of $(\overline{u_s t}/T)/(\overline{u_s u_s}/U)$ in the square and diamond ducts are shown in Figs. 28 and 29, respectively. In both ducts, the value is nearly constant and is close to 1, although the value reaches the local maximum and then decrease rapidly to zero near the corner in the square duct and near Corner A with acute angle. As mentioned in section 3.6, in the square duct, $c_{\mu ss}$ and $c_{\mu nn}$ have very large values at $x_2^+, x_3^+ \le 70$ . However, $(\overline{u_s t}/T)/(\overline{u_s u_s}/U)$ becomes only slightly larger than that near the corner. The reason is that the effect of walls on the flow field is similar to that on the temperature field. Considering the circumstances mentioned above, it is expected to be able to predict the turbulent heat fluxes in the square and diamond ducts by using the ratio of $(\overline{u_s t}/T)/(\overline{u_s u_s}/U)$, once the Reynolds stresses are predicted accurately.

Finally, the production terms of turbulent heat fluxes are examined in the generalized coordinate system. The production terms, $P_{i\theta}$ , are written as:

$$P_{i\theta} = -\overline{u_i u_j}\frac{\partial T}{\partial x_j} - \overline{u_j t}\frac{\partial U_i}{\partial x_j} \tag{7}$$

When the $x_s$ and $x_h$ directions completely align, $P_{i\theta}$ becomes

$$P_{h\theta} = P_{s\theta} = -\overline{u_s u_s}\frac{\partial T}{\partial x_s} - \overline{u_s t}\frac{\partial U_s}{\partial x_s} \tag{8}$$

This term depends only on the $x_s$-direction components, $\overline{u_s u_s}$, $\overline{u_s t}$, $\partial U_s / \partial x_s$ and $\partial T / \partial x_s$. Note that $P_{i\theta}$ is very similar to $P_{ss}$ (Eq. (4)). This is a main reason reasons why $(\overline{u_s t}/T)/(\overline{u_s u_s}/U)$ is nearly constant.

When the $x_s$ and the $x_h$ directions do not align, e.g., the case at a very small Prandtl number, only $P_{i\theta}$ in the $x_h$ direction,

$$P_{h\theta} = -\overline{u_h u_j}\frac{\partial T}{\partial x_j} - \overline{u_h t}\frac{\partial U_h}{\partial x_h} \tag{9}$$

is considered. The first term on the right side of Eq. (9) consists of the Reynolds stresses $\overline{u_h u_j}$ and the mean temperature gradients. Once the Reynolds stresses are predicted accurately, it is possible to evaluate the effect of each directional mean temperature gradient on $P_{h\theta}$. The last term in Eq. (9) consists of only the mean velocity gradient $\partial U_h / \partial x_h$ and $\overline{u_h t}$ itself. Therefore, it is expected that $\overline{u_h t}$ is written as a function of $\partial U_h / \partial x_h$ in the $x_h$- direction plus the effect of mean temperature gradients. The resulting model is likely to be simpler than that in the Cartesian coordinate system, although it is necessary to determine the $x_h$-direction.

## 4. Conclusions

We have simulated the fully developed turbulent velocity and temperature fields in square and diamond ducts to examine the effects of walls. The diamond duct is the most efficient for heat transfer among the circular, square and diamond ducts. The dissimilarity between momentum and heat transfer in the diamond duct is stronger than that in the square duct. For designing thermal mechanical equipment, the duct that has obtuse-angle corners is more efficient than that of acute-angle corners.

We propose the use of a generalized coordinate system, where the three normal directions are defined by referring to the principal axes of the Reynolds stress tensor. It is expected that the eigenvectors of Reynolds stresses can be easily determined particularly near the wall through geometrical configurations. It is because they have a relatively universal property near the wall even in ducts with complex wall boundaries, such as square and diamond ducts. With this coordinate system, it is sufficient to model only the normal Reynolds stresses, $\overline{u_s u_s}$ and $\overline{u_n u_n}$, and the turbulent kinetic energy. In addition, it is found that the distributions of $c_{\mu ii}$ are simpler in this generalized coordinate system than in the conventional Cartesian coordinate system. Therefore, it is tactically advantageous to use geometrical configurations to determine the eigenvectors of the Reynolds stresses and to develop a turbulence model in the generalized coordinate system.

We have also examined the direction of turbulent heat flux vector, i.e., $x_h$-direction. At $\mathrm{Pr} \approx 1$, the $x_h$ and $x_s$ directions align very well and the ratio, $(\overline{u_s t}/T)/(\overline{u_s u_s}/U)$, is nearly a constant value of 1. Therefore, it is possible to predict turbulent heat fluxes well once the Reynolds stresses are predicted accurately. Even when the $x_s$ and $x_h$ directions do not align, it is expected that $\overline{u_h t}$ is written as a function of $\partial U_h / \partial x_h$ in the $x_h$ direction plus the effect of mean temperature gradients in a viewpoint of production terms of turbulent heat fluxes, although it is an open question how to determine the $x_h$ direction.


## Acknowledgments

This work was supported through the research project on "Micro Gas Turbine/Fuel Cell Hybrid-Type Distributed Energy System" by the Department of Core Research for Evolutional Science and Technology (CREST) of the Japan Science and Technology Corporation (JST).


## References


Abe, K. and Suga, K.(2001): Towards the development of a Reynolds-averaged algebraic turbulent

scalar-flux model. Int. J. Heat and Fluid Flow. **22**, 19-29

Akselvoll, K. and Moin, P. (1995): Large eddy simulation of turbulent confined coannular jets and turbulent flow over a backward facing step. Rep. TF-**63**, Stanford University

Brundrett, E., and Burroughs, P. R. (1967): The temperature inner-law and heat transfer for turbulent air flow in a vertical square duct. **10**, 1133-1142

Gavrilakis, S. (1992): Numerical simulation of low-Reynolds-number turbulent flow through a straight duct. J. Fluid Mech. **244**, 101-129

Hirota, M., Fujita, H., Yokosawa, H., Nakai, H. and Itoh, H. (1997): Turbulent heat transfer in a square duct. Int. J. Heat and Fluid Flow. **18**, 170-180

Huser, A. and Biringen, S. (1993): Direct numerical simulation of turbulent flow in a square duct. J. Fluid Mech. **257**, 65-95

Kasagi, N. and Iida, O. (1999): Progress in direct numerical simulation of turbulent heat transfer. Proceedings of the 5th ASME/JSME Joint Thermal Engineering Conference, In CD-ROM, March 15-19, San Diego, California.

Kasagi, N., and Ohtsubo, Y. (1993): Direct Numerical Simulation of Low Prandtl Number Thermal Field in a Turbulent Channel Flow. in Turbulent Shear Flows VIII, F. Durst *et al*., eds., Springer-Verlag, Berlin, 97-117.

Kasagi, N., Tomita, Y., and Kuroda, A. (1992): Direct Numerical Simulation of Passive Scalar Field in a Turbulent Channel Flow. ASME J. Heat Transfer, **114**, 598-606.

Kim, J. and Moin, P. (1985): Application of a fractional-step method to incompressible Navier-Stokes equations. J. Comp. Phys. **59**, 308-323

Kuroda, A., Kasagi, N. and Hirata, M. (1990): Investigation of Dynamical Effects of the Mean Shear Rate on the Wall Turbulence via Direct Numerical Simulation. 27th National Heat Transfer Symposium of Japan, Nagoya, 46-48.

Satake, S., Kunugi, T. and Himeno, R. (2000): High Reynolds number computation for turbulent heat transfer in a pipe flow. Proceedings of the 3rd ISHPC, LNCS 1940, M. Valero *et al*., eds., Springer-Verlag, Berlin, 514-523

Spalart, P. R., Moser, R. D. & Rogers, M. M. (1991): Spectral methods for the Navier-Stokes equations with one infinite and two periodic directions. J. Comp. Phys. **96**, 297-324

| | $\mathrm{Re}_b$ | $\mathrm{Re}_\tau$ | $f_0$ | $Nu_0$ | $Nu_0/(f_0\,\mathrm{Re}_b)$ |
|---|---|---|---|---|---|
| Square | 4486 | 301 | 0.0361 | 14.7 | 0.908 |
| Diamond | 4485 | 287 | 0.0327 | 13.7 | 0.934 |
| Circular (Satake, 2000) | 4300 | 300 | 0.0395 | 15.7 | 0.924 |

Table 1 Friction factor and Nusselt number in square, diamond and circular ducts

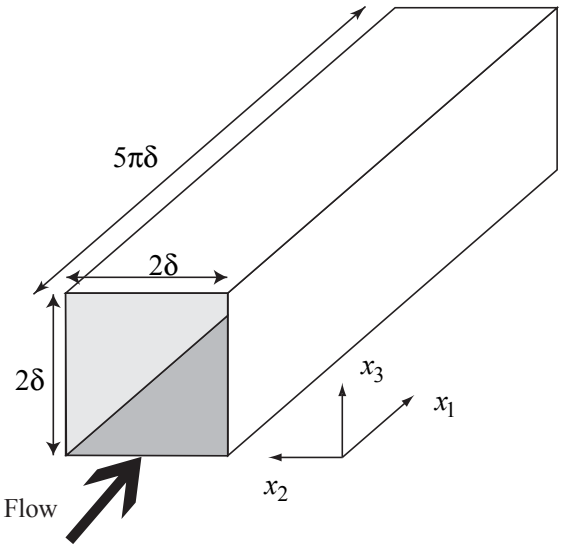


Fig. 1 Coordinate system in a square duct

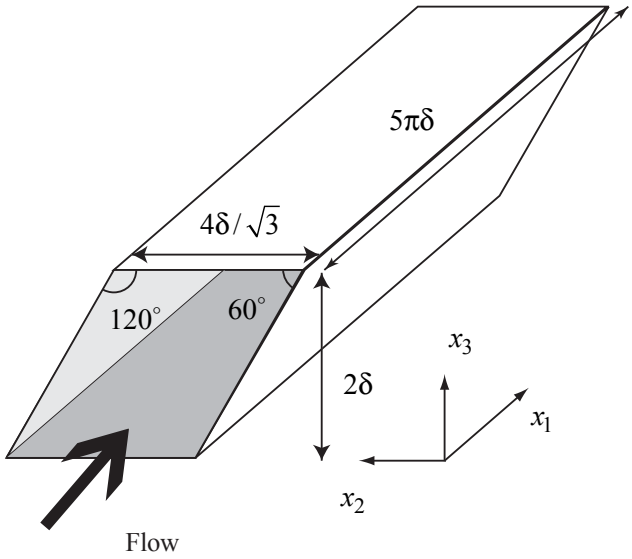


Fig. 2 Coordinate system in a diamond duct

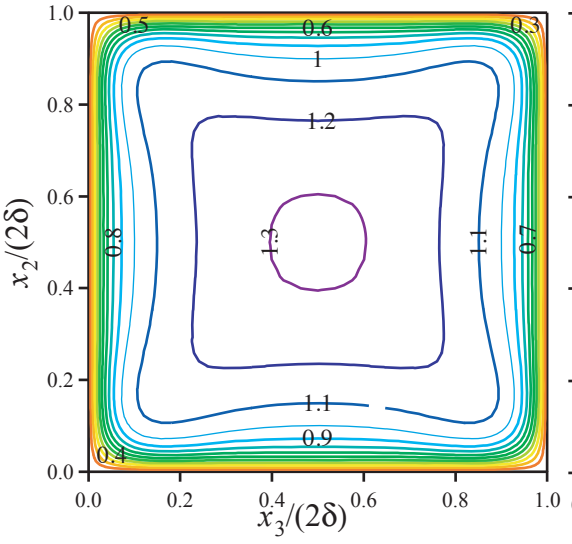


Fig. 3 Mean streamwise velocity, $U/U_b$ in the square duct

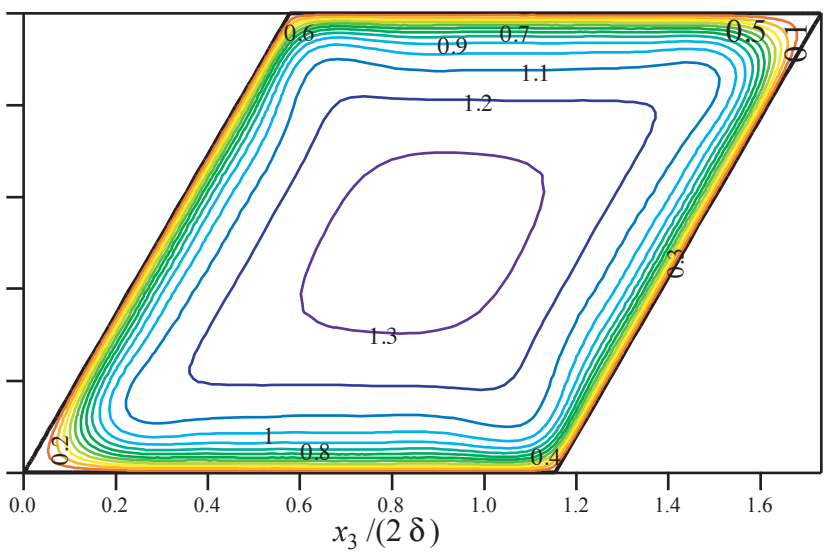


Fig. 4 Mean streamwise velocity, $U/U_b$ in the diamond duct

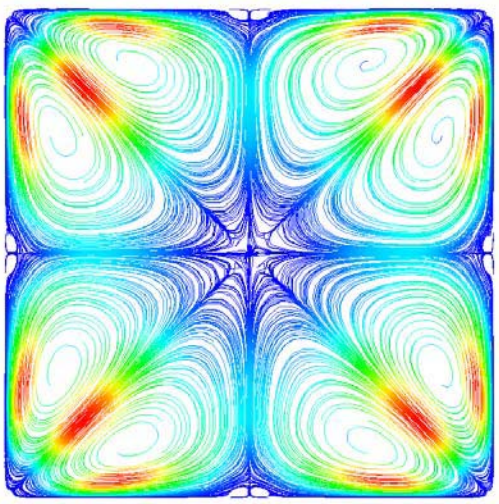

Fig. 5 Streamline of secondary flow in a square duct

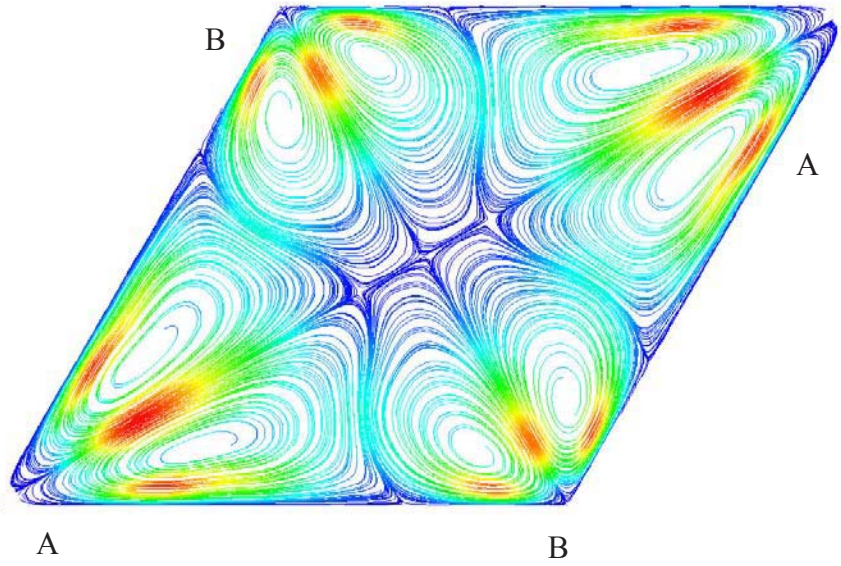


Fig. 6 Streamline of secondary flow in a diamond duct

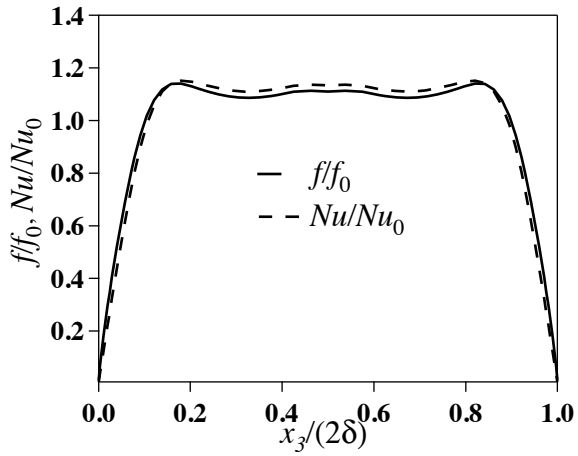


Fig. 7 $f / f_0$ and $Nu / Nu_0$ in the square duct

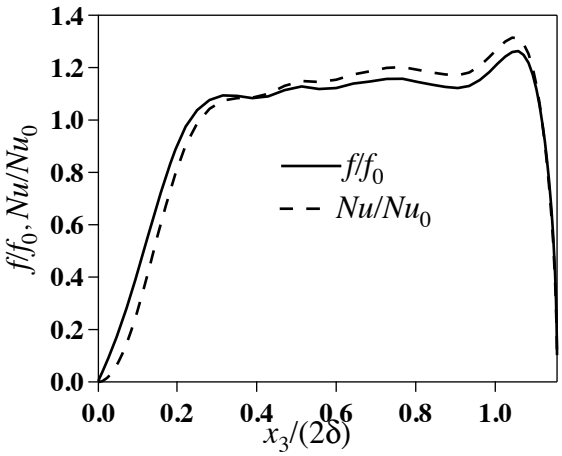


Fig. 8 $f / f_0$ and $Nu / Nu_0$ in the diamond duct

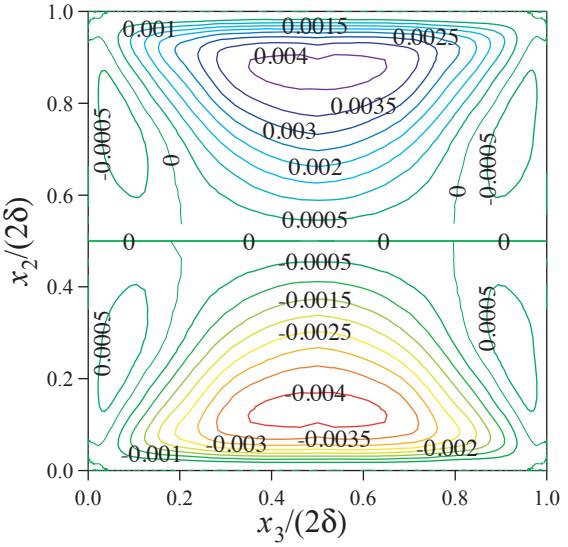


Fig. 9 Turbulent heat flux, $\overline{u_2 t}$, in the square duct

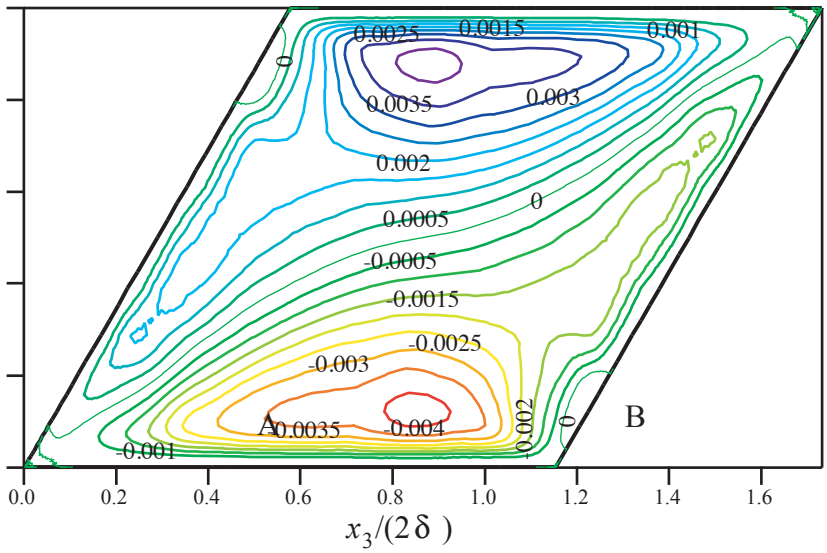


Fig. 10 Turbulent heat flux, $\overline{u_2 t}$, in the diamond duct

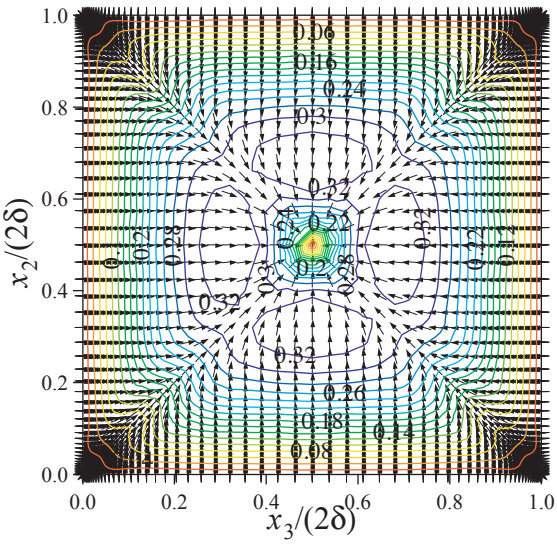


Fig. 11 Eigenvector of $\overline{u_i u_j}$ with the smallest eigenvalue in the square duct

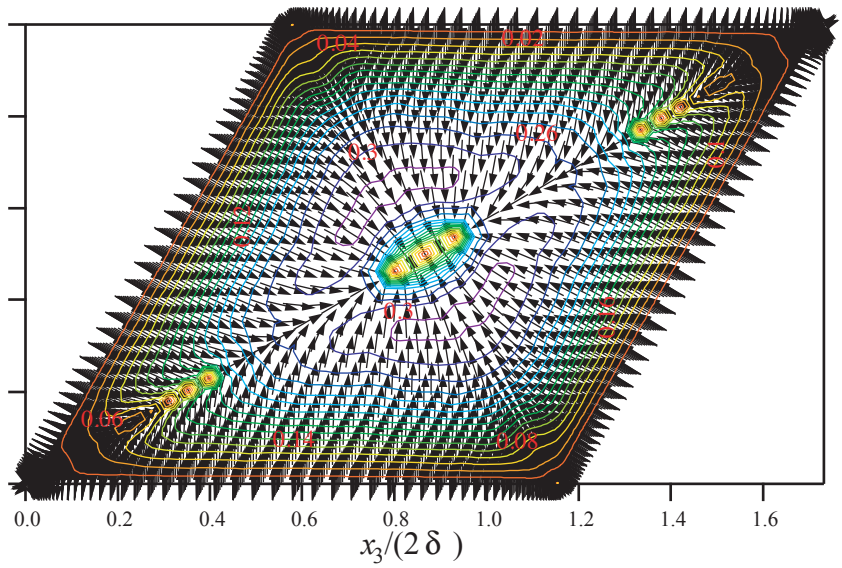


Fig. 12 Eigenvector of $\overline{u_i u_j}$ with the smallest eigenvalue in the diamond duct

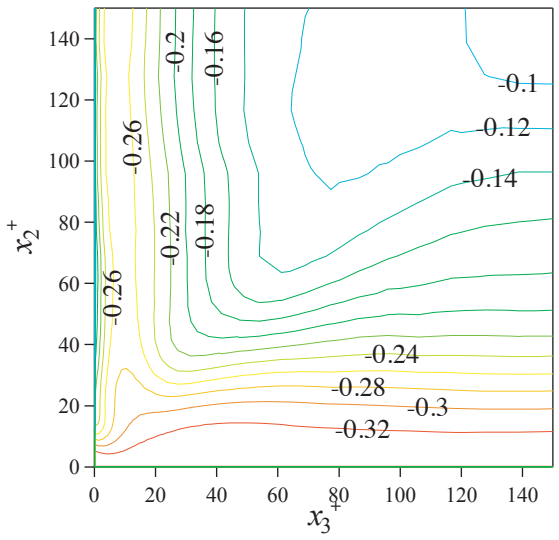


Fig. 13 Anisotropy tensor, $b_{22}$, in the square duct

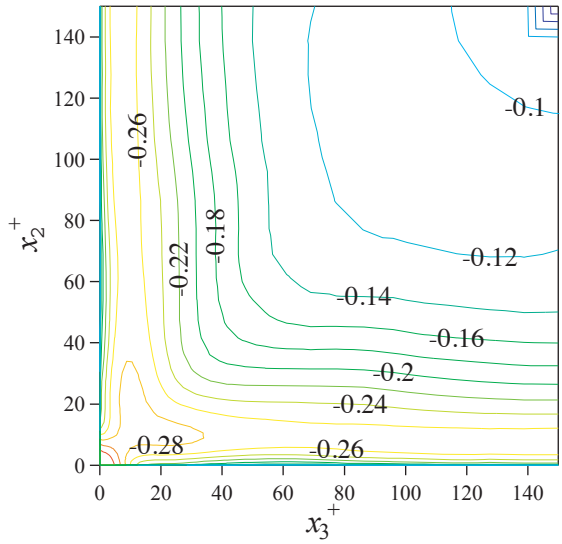


Fig. 14 Anisotropy tensor, $b_{tt}$, in the square duct

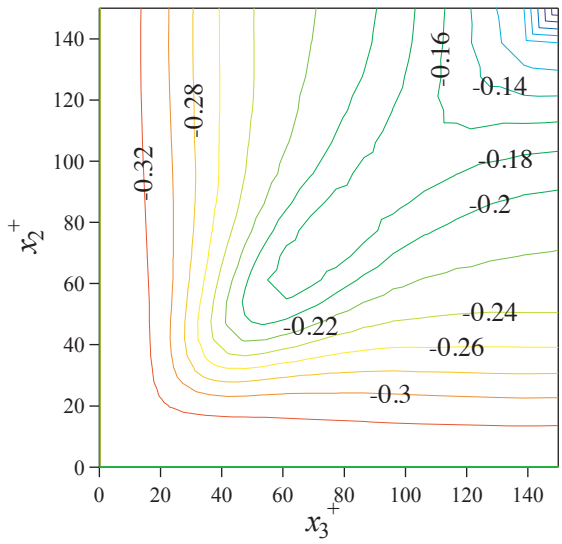


Fig. 15 Anisotropy tensor, $b_{nn}$, in the square duct

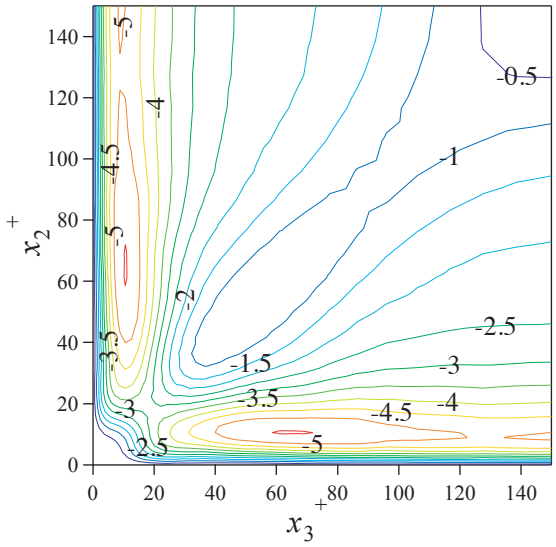


Fig. 16 Mean rate-of-strain, $S_{ss}$, in the square duct

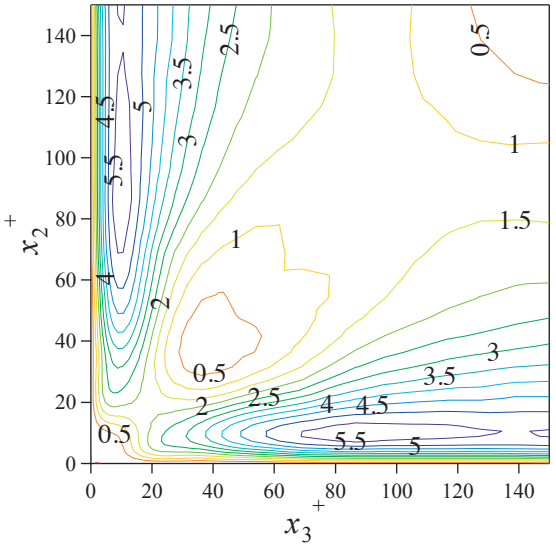


Fig. 17 Mean rate-of-strain, $S_{nn}$, in the square duct

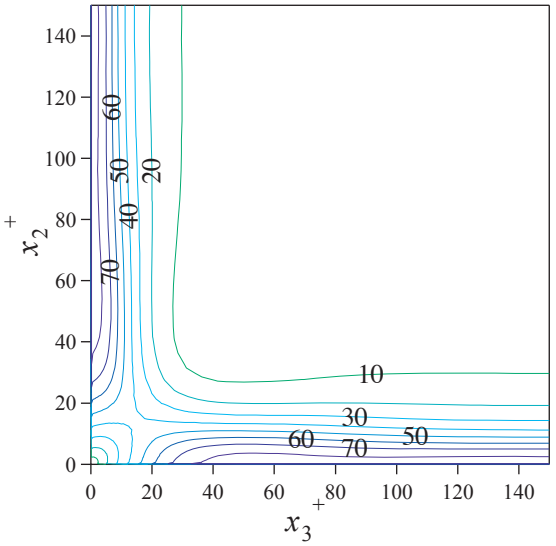


Fig. 18 Mean rate-of-strain, $S_{sn}$, in the square duct

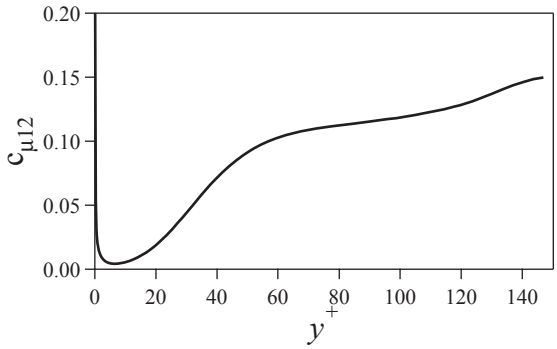


Fig. 19 Distribution of $c_{\mu 12}$ , in the channel

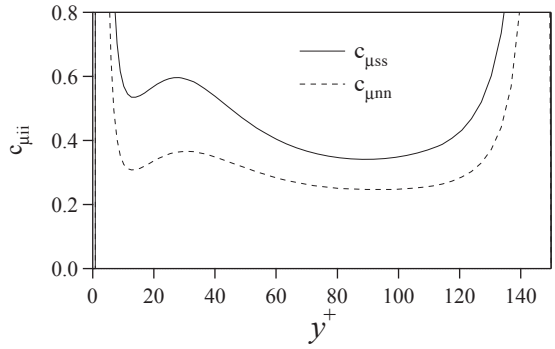


Fig. 20 Distribution of $c_{\mu ss}$ and $c_{\mu ss}$ , in the channel

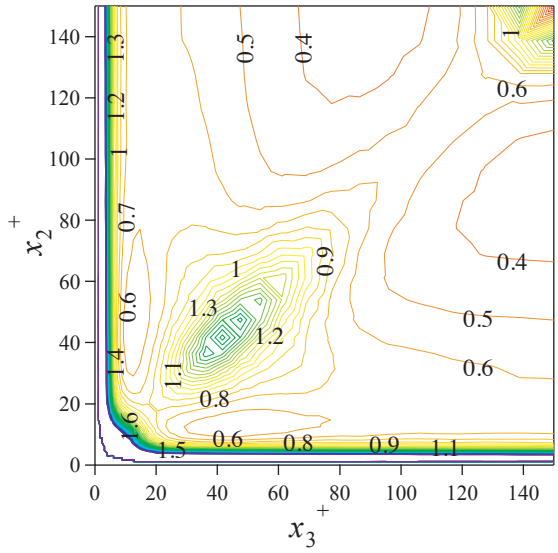


Fig. 21 Distribution of $c_{\mu ss}$ , in the square duct

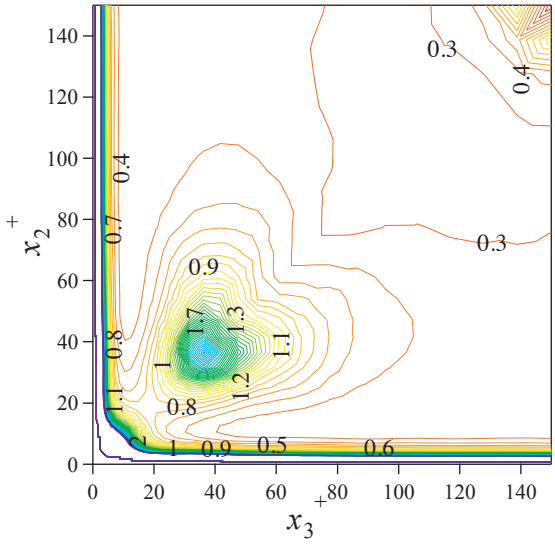


Fig. 22 Distribution of $c_{\mu nn}$ , in the square duct

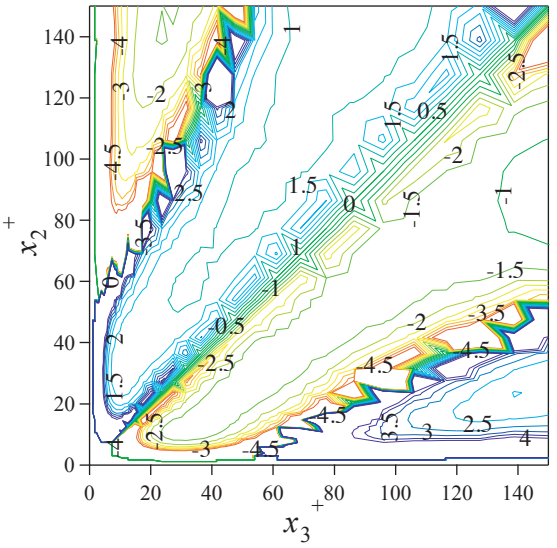


Fig. 23 Distribution of $c_{\mu 22}$ , in the square duct

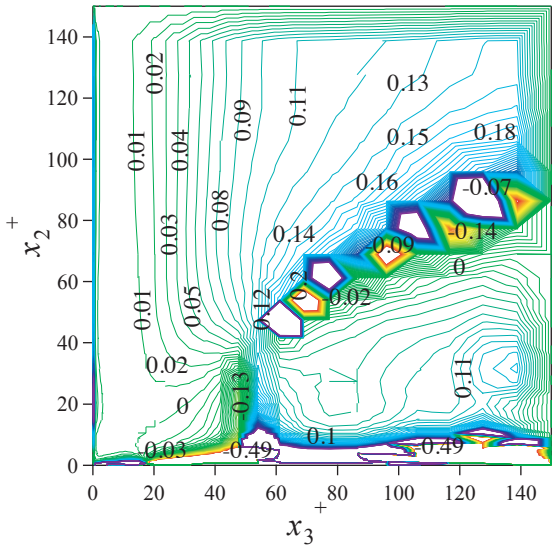


Fig. 24 Distribution of $c_{\mu 13}$ , in the square duct

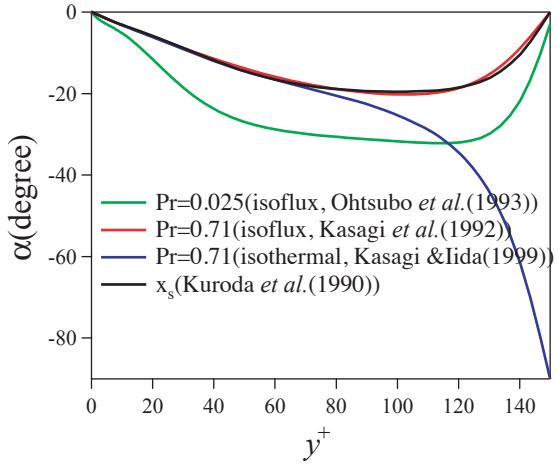


Fig. 25 Distributions of the angle, $\alpha$, between directions of turbulent heat flux vectors and $x_s$-direction with the largest eigenvalue in the channel

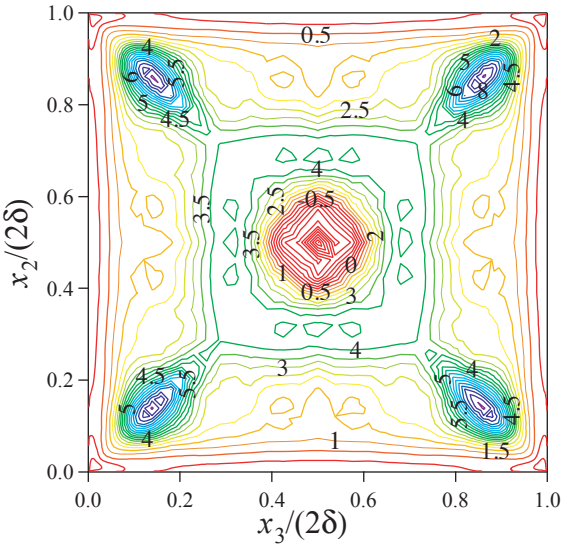


Fig. 26 Distributions of the angle, $\alpha$, between $x_s$- and $x_h$-directions in the square duct

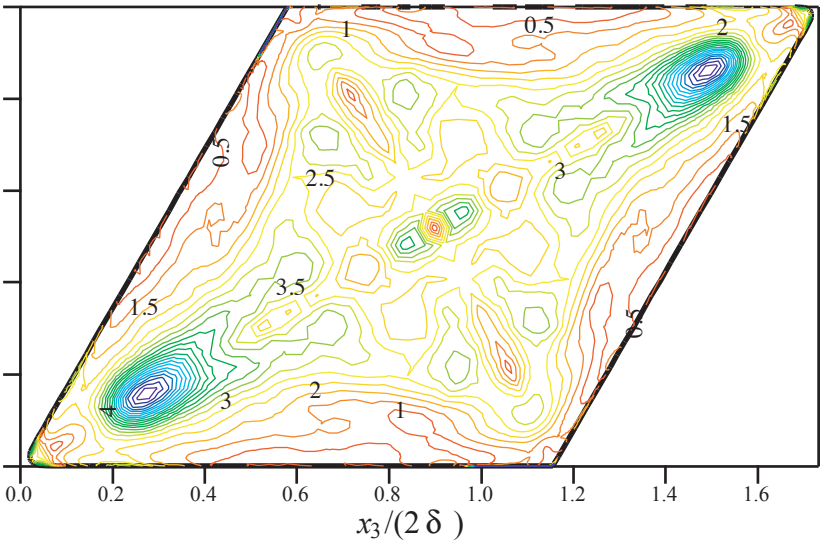


Fig. 27 Distributions of the angle, $\alpha$, between $x_s$- and $x_h$-directions in the diamond duct

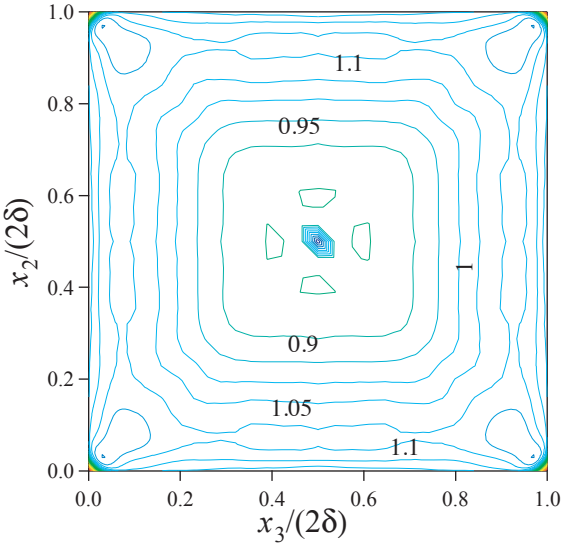


Fig. 28 Distribution of $(\overline{u_s t}/T)/(\overline{u_s u_s}/U)$ in the square duct

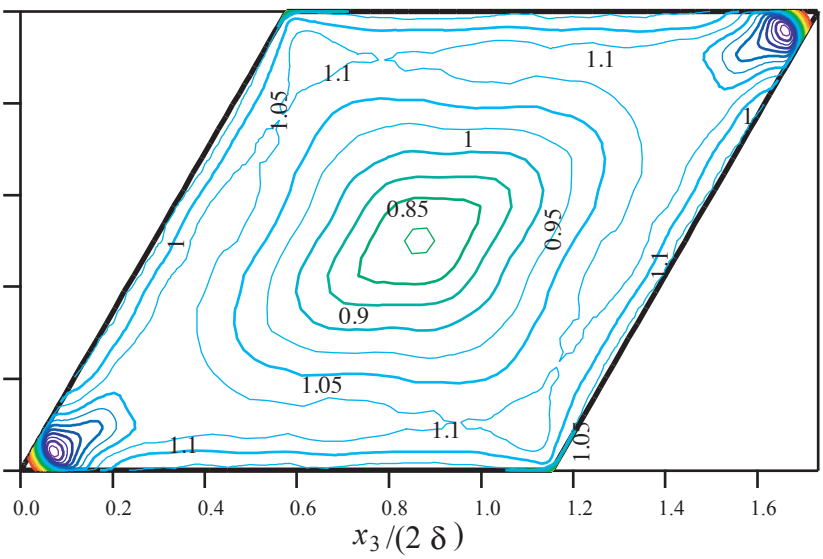


Fig. 29 Distribution of $(\overline{u_s t}/T)/(\overline{u_s u_s}/U)$ in the diamond duct